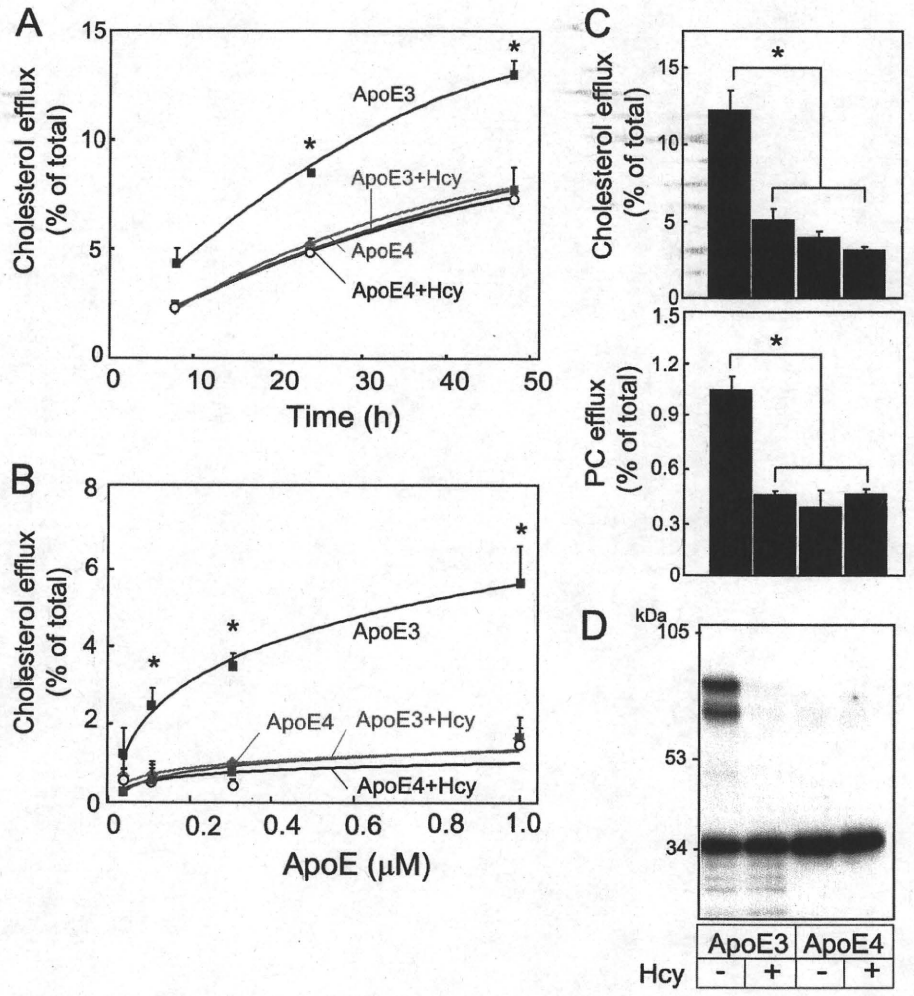

FIGURE 2. **Impairment of apoE3 function by Hcy in cultured neurons.** *A*, the cultured neurons labeled with [^{14}C]acetate were exposed to apoE3 (*blue squares*), apoE3+Hcy (*red squares*), apoE4 (*green circles*), and apoE4+Hcy (*open circles*) for various times at 0.3 μM apoE. The lipids released into the media and the lipids retained in the cells were determined. Data are means ± S.E. of four samples. *, $p < 0.001$ *versus* apoE3+Hcy, apoE4, and apoE4+Hcy at each dose point. *B*, each culture was exposed to apoE3 (*blue squares*), apoE3+Hcy (*red squares*), apoE4 (*green circles*), and apoE4+Hcy (*open circles*) at 0.05, 0.01, 0.3, and 1.0 μM for 24 h. The percentages of released cholesterol and PC levels with respect to the total levels were calculated. Data are means ± S.E. of four samples. *, $p < 0.001$. Three independent experiments showed similar results. *C*, the levels of cholesterol and PC efflux were determined in neuron cultures treated with apoE3, apoE3+Hcy, apoE4, and apoE4+Hcy 24 h after the commencement of treatment of apoEs at 0.3 μM. The percentages of released cholesterol and PC levels over the total levels were calculated. Data are means ± S.E. of four samples. *, $p < 0.0001$. Three independent experiments showed similar results. *D*, Western blot analysis of the samples of apoE3, apoE3+Hcy, apoE4, and apoE4+Hcy was performed under nonreducing conditions.

the commencement of treatment of apoEs at 0.3 μM (Fig. 2*A*). The levels of cholesterol efflux induced by apoE3 were greater than those induced by apoE3 preincubated with Hcy, apoE4, or apoE4 preincubated with Hcy at 24 and 48 h. We also determined the levels of cholesterol efflux 24 h after the commencement of treatment of apoEs at 0.1, 0.3, and 1.0 μM (Fig. 2*B*). The levels of cholesterol efflux induced by apoE3 were greater than those induced by apoE3 preincubated with Hcy, apoE4, or apoE4 preincubated with Hcy at apoE concentrations of 0.3 and 1.0 μM. Next, we determined the levels of cholesterol and PC efflux and also the assembly state of apoE3 and apoE4. The levels of cholesterol and PC released by apoE3 were significantly greater than those released by apoE4 and by apoE3 and apoE4 pretreated with Hcy 24 h after the commencement of treatment (Fig. 2*C*). A reduced level of lipid efflux was accompanied by a reduced level of apoE3 dimers in apoE3 samples pretreated with Hcy (Fig. 2*D*). ApoE4 does not form dimers, owing to a lack of cysteine and Hcy pretreatment dis not affect the apoE4 assembly state.

Regarding the underlying molecular mechanism, we determined whether Hcy and apoE3 form disulfide bonds. We performed reverse-phase HPLC and MS of apoE3-derived peptides, LGADMEDVCGR (residues 104–114) and the Hcy-bound form of LGADMEDVCGR, namely LGADMEDVC(Hcy)GR. The HPLC profiles of the synthetic peptides LGADMEDVCGR and LGADMEDVC(Hcy)GR are shown in Fig. 3*A*, *panels a* and *b*, respectively. We also analyzed LGADMEDVCGR incubated with (Fig. 3*A*, *panel d*) or without Hcy (Fig. 3*A*, *panel c*) for 24 h at 4 °C. The LGADMEDVCGR peptides incubated with Hcy (*peaks 4* and *5*) eluted at positions corresponding to those of LGADMEDVCGR (*peak 1*) and LGADMEDVC(Hcy)GR (*peak 2*), respectively. Peaks 1–5 shown in Fig. 3*A* were analyzed by MALDI-TOF MS. A signal in peak 4 corresponds to the same molecular mass of LGADMEDVC(Hcy)GR (Fig. 3*B*, *4*) as peak 2 (Fig. 3*B*, *2*). A signal in peak 5 corresponds to the same molecular mass of LGADMEDVCGR (Fig. 3*B*, *5*) as peak 1 (Fig. 3*B*, *1*). Signals in peak 3 correspond to LGADMEDVCGR and LGADMEDVCGR dimers (Fig. 3*B*, *3*). Some of the dimers dissociate into monomers by laser irradiation during MS. These data also show that the LGADMEDVCGR peptides tend to form dimers by disulfide bonds in an environment susceptible to oxidation; however, in the presence of Hcy, Hcy inhibited the dimer formation by direct interaction with the thiol of Cys residues.

Next, we analyzed the interaction between intact apoE3 and Hcy. The solution containing intact apoE3 was incubated with or without Hcy at 4 °C for 1 day. ApoE3 in the solution was digested with trypsin, and the tryptic peptides of intact apoE3 incubated with (Fig. 3*C*, *panel e*) or without (Fig. 3*C*, *panel d*) Hcy were analyzed by HPLC. The level of peak 3 (Fig. 3*C*, *panel e*), which has the same elution time as LGADMEDVC(Hcy)GR (Fig. 3*C*, *panel b*), increased compared with that of peak 1 (Fig.

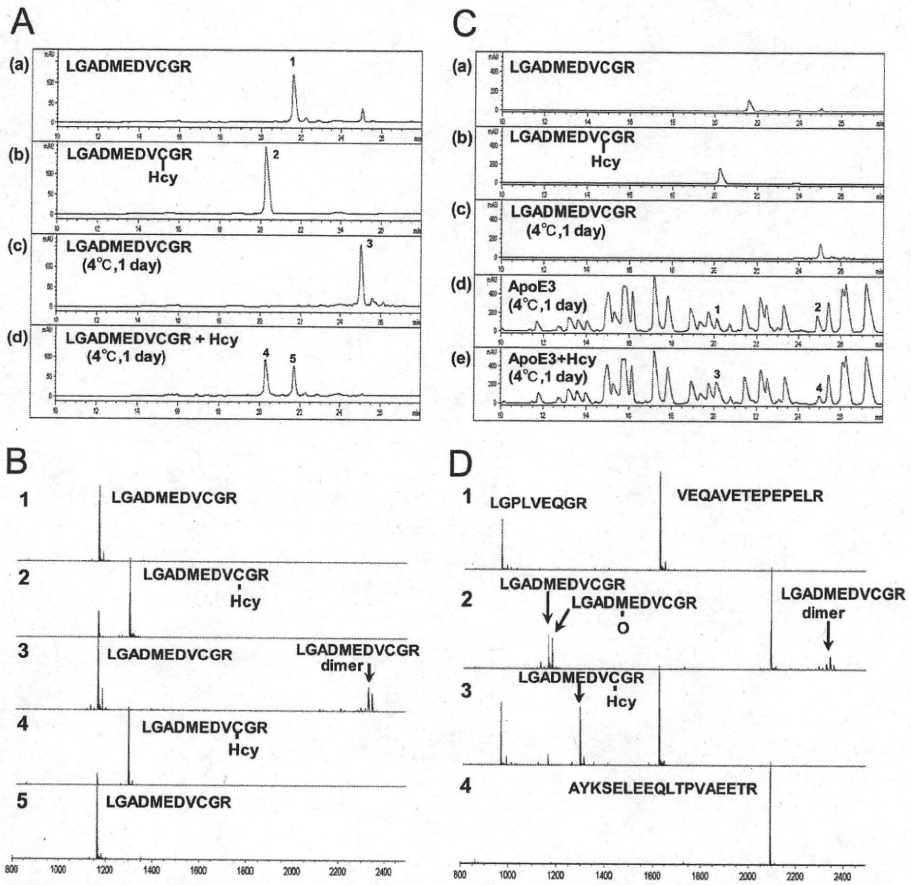

FIGURE 3. **Reverse-phase HPLC profiles and MS of apoE3-derived peptides.** *A*, LGADMEDVCGR peptides (*panel a*), LGADMEDVC(Hcy)GR peptides (*panel b*), and LGADMEDVCGR peptides incubated at 4 °C for 1 day with (*panel d*) or without (*panel c*) Hcy were subjected to HPLC. *B*, peaks 1–5 as shown in Fig. 3*A* were subjected to MALDI-TOF MS using α-cyano-4-hydroxycinnamic acid as a matrix. *C*, the tryptic peptides of intact recombinant apoE3 incubated at 4 °C for 1 day with or without Hcy were analyzed by HPLC. Elution profiles of LGADMEDVCGR (*panel a*), LGADMEDVC(Hcy)GR (*panel b*), and LGADMEDVCGR peptides incubated at 4 °C for 1 day (*panel c*), and tryptic peptides of incubated apoE3 with (*panel e*) or without (*panel d*) Hcy are shown. The elution conditions were the same as those described in *A*. *D*, *peaks 1* and *3*, which correspond to LGADMEDVC(Hcy)GR in *C*, *panel b*, and *peaks 2* and *4*, which correspond to LGADMEDVCGR dimers in Fig. 3*C*, *panel c*, were subjected to MS.

TABLE 1

The profiles of patients examined

Patient Nos. 1–6 were diagnosed as hyperhomocysteinemia and Nos. 7 to 12 were diagnosed as normal plasma Hcy. VD, vascular dementia; NPH, normal pressure hydrocephalus; SD-NFT, senile dementia of neurofibrillary tangle type; DLB, dementia with Lewy body disease; CVD, cerebrovascular disease; PSP, progressive supranuclear palsy.

No.	Age	Sex	Diagnosis	Serum Hcy	CSF Hcy
				μM	nM
1	89	F	CVD	50.4	0.90
2	75	F	CVD	1192	61.8
3	96	F	AD	45.5	1.14
4	89	F	DLB	43.8	56.2
5	71	M	PSP	25.8	0.40
6	91	F	CVD	38.0	0.6
7	81	M	VD	3.7	1.23
8	86	F	AD	5.0	0.43
9	83	F	AD	1.4	0.32
10	95	F	SD-NFT	5.7	0.32
11	84	M	NPH	6.7	0.20
12	79	M	DLB	1.9	0.22

3*C*, *panel d*), whereas that of peak 4 (Fig. 3*C*, *panel e*), which has the same elution time as LGADMEDVCGR (Fig. 3*C*, *panel c*), decreased compared with that of peak 2 (Fig. 3*C*, *panel d*).

Furthermore, peaks 1–4, shown in Fig. 3*C*, were also analyzed by MS (Fig. 3*D*). The signals in peak 1 correspond to LGPLVEQGR (residues 181–189) and VEQAVETEPEPELR (residues 2–15) (Fig. 3*D*, *peak 1*). The signals in peak 3, which has the same elution time as peak 1, correspond to LGADMEDVC(Hcy)GR, indicating that intact apoE3 binds to Hcy in addition to LGPLVEQGR and VEQAVETEPEPELR (Fig. 3*D*, *peak 3*). The signals in peak 2, which has the same elution time as peak 4, correspond to LGADMEDVCGR and LGADMEDVCGR dimer in addition to AYKSELEEQLTPVAEETR (residues 73–90) (Fig. 3*D*, *peak 2*).

Next, we examined whether the ratio of the apoE3 dimer is lower in the human subjects with hyperhomocysteinemia than in human subjects with normal Hcy. The CSF from human apoEε3/3 carriers with normal plasma Hcy and hyperhomocysteinemia were analyzed. The profiles of patients are shown in Table 1. The Hcy concentrations in the plasma and CSF from the patients with hyperhomocysteinemia were higher (mean ± S.E., 232.58 ± 191.91 μM for plasma and 20.17 ± 12.30 nM for CSF, Table 1) than those from the patients with normal plasma Hcy (4.07 ± 0.86 μM for plasma and 0.45 ± 0.16 nM for CSF, Table 1). The results of Western blot analysis of these samples under nonreducing conditions are shown in Fig. 4*A*. The band signals of apoE3 dimers and monomers were scanned by densitometry, and the ratio of the levels of dimers with respect to the level of total apoE3 was calculated. The ratio of the levels of apoE3 dimers with respect to the level of total apoE3 is significantly lower in those who have hyperhomocysteinemia (Fig. 4*B*). The CSF samples from the human subjects with hyperhomocysteinemia contain a higher level of Hcy (mean ± S.E. = 20.17 ± 12.30 nM, Table 1) compared with those from the human subjects with normal plasma Hcy (0.45 ± 0.16 nM, Table 1), suggesting that a larger amount of Hcy binds apoE3 molecules via disulfide bonds and inhibits apoE3 dimerization. The correlation between the level of Hcy and the ratio of apoE3 dimer is shown in supplemental Fig. 2. Dimer ratios tended to negatively correlate with Hcy level in CSF and serum samples, although it does not reach statistical significance (supplemental Fig. 1, *A* and *B*). This tendency for a negative correlation becomes stronger when the separately distributed data (a, b, or c) are removed. The serum lipid profiles of the patients and the correlations of the lipid

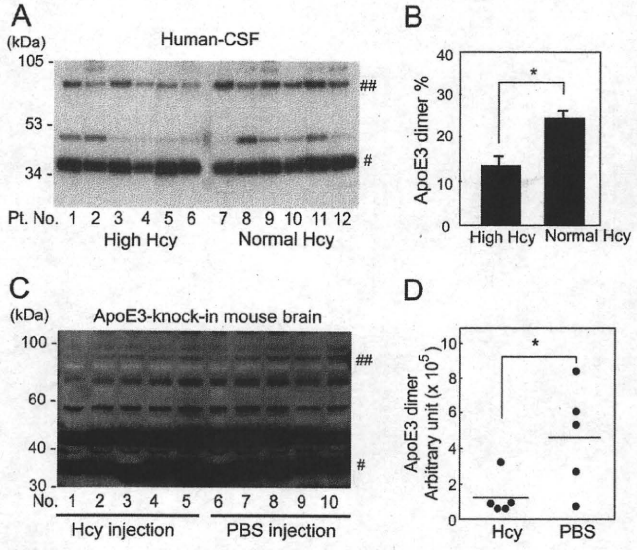

FIGURE 4. **Assembly state of apoE3 in the CSF from human subjects with normal plasma Hcy and hyperhomocysteinemia.** *A*, CSF from human subjects with hyperhomocysteinemia or normal plasma Hcy was mixed with an equal amount of sampling buffer consisting of 100 mM Tris-HCl (pH 7.4), 10% glycerol, 4% SDS, and 0.01% bromphenol blue, and analyzed using 12.5% Tris/Tricine SDS-PAGE under nonreducing conditions. The proteins transferred to the membrane were subjected to Western blot analysis using the anti-apoE antibody. # and ##, apoE3 monomers and dimers, respectively. *Pt. No.*, patient number. *B*, the ratio of signal intensities of apoE dimers with respect to total apoE (monomers plus dimers) in each sample was determined by densitometry and calculation. The values are means ± S.E. of six CSF samples from human subjects with high and normal plasma Hcy. *, $p < 0.003$. *C*, Western blot analysis of brain homogenate prepared from apoE3 knock-in mice subcutaneously injected with Hcy. *Numbers 1–5* are the samples from mice treated with Hcy, and *numbers 6–10* are those from mice treated with PBS. # and ##, the apoE3 monomers and dimers, respectively. *D*, quantification of signals representing the apoE3 dimer in *D* is determined by densitometry. The values are means ± S.E. of five brain homogenate samples. *, $p < 0.005$.

profiles and the ratio of apoE3 dimer are also shown in supplemental Table 1 and supplemental Fig. 3.

We next examined whether hyperhomocysteinemia inhibits apoE3 dimer formation in the brains of mice expressing human apoE3 without expressing rodent endogenous apoE. ApoE3 knock-in mice were injected with 100 μl of 0.6 μM Hcy subcutaneously twice a day for 6 days. The mice were then sacrificed, brains and serum were isolated, and the level of the apoE3 dimer in brain samples was determined by Western blot analysis under nonreducing conditions. The level of the apoE3 dimer in each sample that was loaded with equal amounts of brain homogenate protein is shown in Fig. 4, *C* and *D*. The Hcy level in the serum from the Hcy-injected mice is significantly higher than those from PBS-injected mice (mean ± S.E. for Hcy-treated samples is 10.26 ± 0.47 μM and that for control is 4.98 ± 0.48 μM; $p < 0.0001$). The level of the apoE3 dimer is significantly lower in Hcy-injected mouse brains than in control brains (Fig. 4*D*). Although the ratio of the apoE3 dimer in the mouse brain was very low compared with that of human CSF, these results show that a higher level of serum Hcy resulted in the attenuation of dimer formation of apoE3 in the brain.

DISCUSSION

Our previous studies have shown that intramolecular interaction (*i.e.* domain interaction) and intermolecular interaction

TABLE 2
Association of Hcy with apoE3 and apoE4

To determine the association of Hcy with apoE, 7.5 μl of 100 mM Hcy was added to 500 μl of apoE-containing solution at 14.7 mM apoE. The apoE3 and apoE4 containing solutions with or without Hcy, or Hcy solution without apoE were incubated overnight at room temperature. The solutions were then dialyzed against PBS overnight at room temperature, and the level of Hcy in each solution was determined. UD, under detectable level.

	Hcy ($n = 8$)	apoE3 ($n = 3$)	apoE4 ($n = 3$)	apoE3 + Hcy ($n = 8$)	apoE4 + Hcy ($n = 8$)
Hcy (μM)	UD	UD	UD	5.75 ± 0.25	UD

(*i.e.* dimerization) determine the apoE isoform-dependent ability to generate HDL (7, 10). Because Hcy is a molecule harboring a thiol, we hypothesized that the thiol of Hcy associates with the thiol of cysteine residues in apoE3, and the formation of this disulfide bonds interferes with apoE3 dimerization. In the present study, we found that Hcy binds to cysteine residues of apoE3, thereby interfering with apoE3 dimerization and impairing the ability of apoE3 to generate HDL to a level similar to that of apoE4. These *in vitro* results are supported by those of the analysis of human CSF samples from patients with hyperhomocysteinemia and normal serum homocysteine, showing that the ratio of the levels of apoE3 dimers with respect to the level of total apoE3 in CSF samples from patients with hyperhomocysteinemia is significantly lower than that from normal controls. In addition, the subcutaneous injection of Hcy into apoE3 knock-in mice resulted in a reduced level of the apoE3 dimer in the brain homogenate, suggesting that hyperhomocysteinemia decreases the level of apoE3 dimer in CSF or the brain.

To determine the effect of Hcy bound to apoE3, we preincubated Hcy and apoE3 at relatively high concentrations. Under these conditions, ~66% of apoE3 binds to Hcy, whereas the level of Hcy bound to apoE4 was not detected (Table 2). One may question whether the inhibitory effect of Hcy on apoE3 dimerization and apoE3-mediated lipid efflux were observed when lower concentrations of Hcy similar to those in serum or CSF were used in the presence of comparable concentrations of apoE3 in culture. Hcy at lower concentrations did not inhibit apoE3 dimerization nor attenuate apoE3-mediated lipid efflux. This may be because it takes a longer time to form disulfide bonds between Hcy and apoE3 at physiological concentrations in culture. However, this is not the case for *in vivo* conditions, including those in human CSF and the mouse brain. Although the precise mechanism underlying this discrepancy cannot be provided by the current study, the disulfide bonds between apoE3 and Hcy molecules occurs *in vivo* at concentrations lower than those used in *in vitro* experiments. In support of this notion, previous studies have shown that >70% of Hcy in plasma forms disulfide-bonded to cysteine residues of proteins including transthyretin (31, 32), suggesting that Hcy at single digit μM concentrations forms disulfide bonds to cysteine residues *in vivo*.

Previous studies have shown other biological and pathological effects of Hcy; namely, Hcy induces neuronal damage (33, 34), compromises blood-brain barrier integrity (26), modulates Aβ toxicity (35), and modulates Aβ generation (27, 28). However, the molecular mechanism(s) by which Hcy directly interacts with the molecule(s) in these studies are not fully understood. In this study, we showed that a high level of Hcy impairs

apoE3 function to a similar level of apoE4 by preventing/breaking the disulfide bonds, thereby leading to a decreased HDL generation. Because apoE-HDL plays a role in Aβ clearance(13,14), the lines of evidence suggest that two different risk factors for AD, apoE4 and hyperhomocysteinemia, may share a common mechanism; that is, apoE4 has a lower ability to generate HDL than apoE3 and the Hcy-induced modification of apoE3 impairs the ability of apoE3 to generate HDL to a level similar to that of apoE4. Our observations in the present study also provide new insight into concerning the apoE genotype-dependent treatment of hyperhomocysteinemia, especially for reducing the risk of AD.

REFERENCES

1. Strittmatter, W. J., Saunders, A. M., Schmechel, D., Pericak-Vance, M., Enghild, J., Salvesen, G. S., and Roses, A. D. (1993) *Proc. Natl. Acad. Sci. U.S.A.* **90,** 1977–1981
2. Krimbou, L., Denis, M., Haidar, B., Carrier, M., Marcil, M., and Genest, J., Jr. (2004) *J. Lipid Res.* **45,** 839–848
3. DeMattos, R. B., Brendza, R. P., Heuser, J. E., Kierson, M., Cirrito, J. R., Fryer, J., Sullivan, P. M., Fagan, A. M., Han, X., and Holtzman, D. M. (2001) *Neurochem. Int.* **39,** 415–425
4. Hara, M., Matsushima, T., Satoh, H., Iso-o, N., Noto, H., Togo, M., Kimura, S., Hashimoto, Y., and Tsukamoto, K. (2003) *Arterioscler. Thromb. Vasc. Biol.* **23,** 269–274
5. Altenburg, M., Johnson, L., Wilder, J., and Maeda, N. (2007) *J. Biol. Chem.* **282,** 7817–7824
6. Michikawa, M., Fan, Q. W., Isobe, I., and Yanagisawa, K. (2000) *J. Neurochem.* **74,** 1008–1016
7. Gong, J. S., Kobayashi, M., Hayashi, H., Zou, K., Sawamura, N., Fujita, S. C., Yanagisawa, K., and Michikawa, M. (2002) *J. Biol. Chem.* **277,** 29919–29926
8. Xu, Q., Brecht, W. J., Weisgraber, K. H., Mahley, R. W., and Huang, Y. (2004) *J. Biol. Chem.* **279,** 25511–25516
9. Gong, J. S., Morita, S. Y., Kobayashi, M., Handa, T., Fujita, S. C., Yanagisawa, K., and Michikawa, M. (2007) *Mol. Neurodegener.* **2,** 9
10. Minagawa, H., Gong, J. S., Jung, C. G., Watanabe, A., Lund-Katz, S., Phillips, M. C., Saito, H., and Michikawa, M. (2009) *J. Neurosci. Res.* **87,** 2498–2508
11. Huang, Y., Liu, X. Q., Wyss-Coray, T., Brecht, W. J., Sanan, D. A., and Mahley, R. W. (2001) *Proc. Natl. Acad. Sci. U.S.A.* **98,** 8838–8843
12. Nakamura, T., Watanabe, A., Fujino, T., Hosono, T., and Michikawa, M. (2009) *Mol. Neurodegener.* **4,** 35
13. Deane, R., Sagare, A., Hamm, K., Parisi, M., Lane, S., Finn, M. B., Holtzman, D. M., and Zlokovic, B. V. (2008) *J. Clin. Invest.* **118,** 4002–4013
14. Jiang, Q., Lee, C. Y., Mandrekar, S., Wilkinson, B., Cramer, P., Zelcer, N., Mann, K., Lamb, B., Willson, T. M., Collins, J. L., Richardson, J. C., Smith, J. D., Comery, T. A., Riddell, D., Holtzman, D. M., Tontonoz, P., and Landreth, G. E. (2008) *Neuron* **58,** 681–693
15. Kolovou, G. D., and Anagnostopoulou, K. K. (2007) *Ageing Res. Rev.* **6,** 94–108
16. McCarron, M. O., Delong, D., and Alberts, M. J. (1999) *Neurology* **53,** 1308–1311
17. Guthikonda, S., and Haynes, W. G. (1999) *Curr. Opin. Cardiol.* **14,** 283–291
18. Kim, N. K., Choi, B. O., Jung, W. S., Choi, Y. J., and Choi, K. G. (2003) *Neurology* **61,** 1595–1599
19. Perry, I. J. (1999) *J. Cardiovasc. Risk* **6,** 235–240
20. Seshadri, S., Beiser, A., Selhub, J., Jacques, P. F., Rosenberg, I. H., D'Agostino, R. B., Wilson, P. W., and Wolf, P. A. (2002) *N. Engl. J. Med.* **346,** 476–483
21. Luchsinger, J. A., Tang, M. X., Shea, S., Miller, J., Green, R., and Mayeux, R. (2004) *Neurology* **62,** 1972–1976
22. Ravaglia, G., Forti, P., Maioli, F., Martelli, M., Servadei, L., Brunetti, N., Porcellini, E., and Licastro, F. (2005) *Am. J. Clin. Nutr.* **82,** 636–643
23. Van Dam, F., and Van Gool, W. A. (2009) *Arch. Gerontol. Geriatr.* **48,** 425–430
24. Isobe, C., Murata, T., Sato, C., and Terayama, Y. (2005) *Life Sci.* **77,** 1836–1843
25. Starkebaum, G., and Harlan, J. M. (1986) *J. Clin. Invest.* **77,** 1370–1376
26. Kamath, A. F., Chauhan, A. K., Kisucka, J., Dole, V. S., Loscalzo, J., Handy, D. E., and Wagner, D. D. (2006) *Blood* **107,** 591–593
27. Pacheco-Quinto, J., Rodriguez de Turco, E. B., DeRosa, S., Howard, A., Cruz-Sanchez, F., Sambamurti, K., Refolo, L., Petanceska, S., and Pappolla, M. A. (2006) *Neurobiol. Dis.* **22,** 651–656
28. Zhang, C. E., Wei, W., Liu, Y. H., Peng, J. H., Tian, Q., Liu, G. P., Zhang, Y., and Wang, J. Z. (2009) *Am. J. Pathol.* **174,** 1481–1491
29. Hamanaka, H., Katoh-Fukui, Y., Suzuki, K., Kobayashi, M., Suzuki, R., Motegi, Y., Nakahara, Y., Takeshita, A., Kawai, M., Ishiguro, K., Yokoyama, M., and Fujita, S. C. (2000) *Hum. Mol. Genet.* **9,** 353–361
30. Michikawa, M., Gong, J. S., Fan, Q. W., Sawamura, N., and Yanagisawa, K. (2001) *J. Neurosci.* **21,** 7226–7235
31. Lim, A., Sengupta, S., McComb, M. E., Théberge, R., Wilson, W. G., Costello, C. E., and Jacobsen, D. W. (2003) *J. Biol. Chem.* **278,** 49707–49713
32. Sass, J. O., Nakanishi, T., Sato, T., Sperl, W., and Shimizu, A. (2003) *Biochem. Biophys. Res. Commun.* **310,** 242–246
33. Kruman, II, Kumaravel, T. S., Lohani, A., Pedersen, W. A., Cutler, R. G., Kruman, Y., Haughey, N., Lee, J., Evans, M., and Mattson, M. P. (2002) *J. Neurosci.* **22,** 1752–1762
34. Maler, J. M., Seifert, W., Hüther, G., Wiltfang, J., Rüther, E., Kornhuber, J., and Bleich, S. (2003) *Neurosci. Lett.* **347,** 85–88
35. White, A. R., Huang, X., Jobling, M. F., Barrow, C. J., Beyreuther, K., Masters, C. L., Bush, A. I., and Cappai, R. (2001) *J. Neurochem.* **76,** 1509–1520

認知症評価における認知機能テストの問題点

Psychological tests in the assessment of dementia and MCI

杉下和行(写真)　杉下守弘
Kazuyuki SUGISHITA[1] and Morihiro SUGISHITA[2]
東京大学医学部附属病院精神神経科[1]，新潟リハビリテーション大学[2]

◎認知症の診断，分類，重症度判定のいずれの段階でも認知機能検査が行われている．これは診察に加えて，さらに多くの情報を得るためとか，患者間の比較や，症状の変化をとらえるためなどといわれているが，立証主義の実施のためということを指摘した．また，最近の認知症の評定に関する大きな出来事として，2004年にアメリカではじまったプロジェクト“Alzheimer病神経画像戦略”(ADNI)と“精神疾患の診断・統計マニュアル”(DSM)の改訂の予定がある．これらについて解説し，ADNIの認知機能検査についても紹介した．ADNIでは，軽度Alzheimer病(AD)，軽度認知障害(MCI)および老年健常人(55～90歳)を，除外基準，包含基準および4つの認知検査を用いて診断している．数種類の認知機能検査を用いて認知症の診断に役立てようとしているのが特徴である．また，除外診断を含む除外基準と包含基準の2つを認知検査と併用している点も特徴である．認知症に伴う精神症状の評価として簡易に施行できる神経精神インベントリー質問紙-日本版(NPI-Q-J)の利点を指摘し，DSM-Vでの認知症の精神症状の評価案にも触れた．

Key word　認知症，臨床認知症評価法(CDR)，心理検査，ADNI，DSM-V

立証主義について

認知機能障害がある場合に，正常圧水頭症や脳腫瘍などの神経疾患，大うつ病性障害や統合失調症などの精神疾患がないかという，いわゆる除外診断を行った後に認知症の診断がなされる．つぎに認知症の分類，すなわち認知症がAlzheimer病(AD)なのか，Lewy小体型認知症(DLB)なのか，前頭側頭型認知症(FTD)なのかという認知症の分類が行われ，さらに，認知症の重症度の測定がなされる．軽度認知障害(MCI)も認知症と同様に，除外診断の後にMCIと診断される．ついで，MCIの分類と重症度測定が行われる．

以上に述べた診断，分類，重症度測定のいずれの段階でも認知機能検査が行われている．通常それは，診断，分類，および重症度判定について診察で得られた情報に加えて，より多くの情報を得るためとか，患者間の比較や，症状の変化をとらえるためなどといわれている．一方，心理検査を行ってもあまり意味はないという立場もある．

心理検査が広く行われる理由は情報を多く得られるとか得られないとかの次元の問題ではなく，実は医学における立証主義の現れのためであるということを指摘したい．表1にはPetersenのMCIの基準[7]を記す．この第2項に，「適切な基準値に従って立証された記憶障害(Memory impairment documented to appropriate reference values)」とある．記憶障害は認知機能検査の基準値(得点)によって立証されることが求められているのである．診察により記憶障害があるとわかっただけでは十分でなく，認知機能検査の得点で立証されていなければならないというのである．分類や重症度測定についても同様で，分類や重症度の立証のための証拠として認知機能検査の得点が求められている．

“Alzheimer病神経画像戦略”(ADNI)とDSM-V

2004年，アメリカではじまった研究プロジェク

表 1　1999年MCI基準(Petersen, 2009)[7]

基準
① 記憶障害の訴えがある．情報提供者によって確証されていることが望ましい
② 適切な基準値に従って立証された記憶障害
③ 記憶でない認知領域では本質的に正常な遂行
④ 日常生活の諸活動は一般的に保たれている
⑤ 認知症にかかっていない

ト“Alzheimer 病神経画像戦略”(ADNI)は，軽度AD，MCI 患者，および老年健常人の認知機能検査に新しい試みをしており，この方法は現在，研究，診療，治験における認知機能検査に多大な影響を与えている．日本もこの国際プロジェクトに参加しているので，日本のプロジェクト(J-ADNI)における認知症および MCI の評価法を解説する必要があろう．

また，最近のもうひとつの話題はアメリカ精神医学会の定めた診断指針である“精神疾患の診断・統計マニュアル第 5 版”(DSM-Ⅴ，準備中)で，dementia という専門用語がなくなることをはじめ，認知症の診断について大幅な変更が予定されていることである．そして，ADNI の評価法についての考え方が採用される予定である．

本稿では上記の 2 項目を踏まえて，認知症と MCI の評価における認知検査の現状について具体的に述べたい．

認知症の診断，分類および重症度

1. 診断

認知症の診断に関連する認知機能検査として種々の認知症スクリーニング検査がある．代表的なものは 1975 年に発表された精神状態短時間検査(MMSE)である．この検査で，23 点あるいは 24 点以下の得点をとった者は認知症の可能性があるとされている．MMSE はすでに数種の日本語版が公にされている．しかし，訳が原版に忠実でなかったり日本文化に適応させるあまり過度の改変が行われたりしているので，あらたな日本語版(MMSE-J)が作成された．この版は原版との等価性が高いので，現在，日本の J-ADNI プロジェクトでも使用されている[8]．

使用ご希望の方は J-ADNI の事務局(center@j-adni.org)にご連絡ください．

2. 分類

認知症は AD, DLB, FTD, 脳血管性認知症(VaD)などに分類されている．それぞれ，症状に特徴がある．たとえば，AD ではエピソード記憶の欠落が最初に起こる．DLB ではエピソード記憶は比較的保たれているが，視空間機能の著しい欠落がめだつといった特徴がある．FTD では注意・遂行障害や言語障害，VaD では注意・遂行障害と視空間機能障害がめだつ．

認知機能検査で認知症を AD，DLB，FTD，VaD などに分類することをめざす検査はいまのところないが，分類のひとつである軽度 AD を診断する認知症検査が ADNI で用いられている．これについては後で言及する．

現在行われている方法は各分類に特徴的な症状があるかないか検査をすることである．たとえば，AD に特徴的なエピソード記憶をみるために，Wechsler 記憶検査法一改訂版(WMS-R)の遅延再生課題(論理的記憶)の第 1 項目や，Alzheimer 病評定尺度一認知下位尺度(Alzheimer's Disease Assessment Scale-cognitive subscale：ADAS-Cog)の遅延再生課題が行われる．DBL に特徴的な視空間機能をみるためには，時計の模写課題や ADAS-Cog の構成課題を行う．FTD に特徴的な注意・遂行機能をみるにはトレイルメイキング検査や Wechsler 成人知能検査第 3 版(WAIS-Ⅲ)の符号問題を用い，言語機能をみるにはボストン呼称検査や範疇流暢性課題などを行う．

3. 重症度の測定

認知症の重症度を検査する認知機能検査には 2 種類ある．ひとつは短時間にできるスクリーニング的な検査で，MMSE などはその一例である．30 点中 11〜20 点取れれば中等度の認知障害，0〜10 点ならば重度の障害である．もうひとつは重症度測定を目的とした詳細な検査で，AD についての

表 2　MCIの分類

記憶のみ障害されている	健忘型 MCI(単一領域)
記憶以外に他の領域も障害されている	健忘型 MCI(多数領域)
記憶以外の単一領域が障害されている	非健忘型 MCI(単一領域)
記憶以外の多数領域が障害されている	非健忘型 MCI(多数領域)

検査はあるが，AD 以外の認知症についての検査はない．AD の重症度を測る検査として臨床認知症評価法(CDR)がある．原版に忠実な日本版(CDR-J)が http://www.nur.ac.jp(新潟リハビリテーション大学ホームページ)から入手可能である．

MCIの診断，分類および重症度

20 世紀の末から認知症の前駆症状である MCI が注目されるようになった．認知症の治療については認知症になる前の状態，すなわち MCI の状態での治療の必要性が叫ばれ，このため，MCI の診断，分類および重症度の測定はその重要さを増大させている．

1. 診断

MCI の診断は，表 1 に示した MCI 基準に基づいて行われる．MCI のスクリーニング検査にはモントリオール認知評定法(MoCA)などがある．MCI の詳しい検査には ADNI の検査があるが，これについては後述する．

2. 分類

MCI の分類でもっとも重要なのは健忘型 MCI である．健忘型であるかどうかという点と，4 つの領域(記憶領域，注意・遂行機能領域，視空間機能領域および言語機能領域)のうち 1 つの領域のみ障害されているか，それとも，2 つ以上の領域が障害されているかという点の 2 つを考慮して，4 つの領域(表 2)に分けられる．なお，4 つの領域の測定に使用される検査は，前述の認知症の分類に使用される検査と同じである．

3. 重症度の測定

従来の健忘型 MCI より軽度のものを早期健忘型 MCI とよんでいる．詳細はつぎの項目で述べる．

ADNIの認知機能検査

ADNI では認知機能検査を用いて，①軽度 AD，②健忘型 MCI，③老年健常人(55〜90 歳)に分類している．ADNI の方法には 2 つの特徴がある．第 1 の特徴は 4 つの認知検査を用いて診断していることである．また，第 2 の特徴は認知機能検査だけでなく除外診断を含む除外基準と包含基準を併用していることである．

まず，老年期うつ尺度(短縮版)日本版(GDS-S-J)[9]で 6 点以上の者を分類の対象から除外する．うつ状態の可能性があるからである．そして，GDS-S-J で 5 点以下のものについて，3 つの心理検査〔MMSE，CDR，論理的記憶(logical memory)の 3 つである．これらの検査の日本版の入手法は認知症のところで述べた〕の得点によって，軽度 AD，健忘型 MCI，および老年健常人を定義している(表 3)．軽度 AD は，MMSE で 20〜26 点，CDR は 0.5 か 1 点，論理的記憶は健忘型 MCI と同じで，教育年数が 16 年以上なら 8 点以下，教育年数 8〜15 年なら 4 点以下，教育年数 0〜7 年なら 2 点以下となる．

ADNI の認知機能検査，除外基準および包含基準については，http://www.adni-info.org/の Scientist's Home page から ADNI Procedures Manuals を選べば，その詳細がわかる．

認知症に伴う精神症状

1. 精神科の診断

そもそも精神科では，DSM や ICD といった操作的診断基準が導入される以前には診断名は統一されていなかった．たとえば，イギリスとアメリカでは精神疾患の範囲が異なっており，精神疾患の統計値には相違が生じていた[5]し，世界保健機構の主導で行われた研究では，ロンドンでの診断に比べモスクワとワシントンでのうつ病の範囲は狭く，統合失調症の範囲が広かったという[6]．その後，DSM や ICD が導入され，精神科の診断名の一致率は格段に上昇した．

表 3　4つの心理検査得点による軽度AD，健忘型MCIおよび健常人の分類

	健常人	健忘型 MCI	軽度 AD
MMSE	24〜30 点	24〜30 点	20〜26 点
包括的 CDR	0 点	0.5 点	0.5 点，1 点
CDR(記憶)	すくなくとも 0.5 点		
論理的記憶			
教育年数 16 年以上	9 点以上	8 点以下	8 点以下
8〜15 年	5 点以上	4 点以下	4 点以下
0〜7 年	3 点以上	2 点以下	2 点以下

早期健忘型 MCI とは，MMSE が 24〜30 点，包括的 CDR が 0.5 点，CDR(記憶)がすくなくとも 0.5 点であり，論理的記憶の得点の高いものである．すなわち，教育年数 16 年以上の場合，論理的記憶の得点 9〜11 点，教育年数が 8〜15 年の場合，論理的記憶の得点 5〜9 点，教育年数が 0〜7 年の場合，論理的記憶の得点 3〜6 点である．

従来，認知症に伴う精神症状の範囲や程度は主観的に評価されており，定量的に評価されることは少なかった．認知症に伴う精神症状の評価についても精神科の診断名の決定と同様に標準的な基準が必要であり，過去にさまざまな妥当性と信頼性が確立されたテストが開発されてきた[10]が，いずれも構造化面接や半構造化面接で施行に時間を要したため普及しなかった．

2. 精神症状の認知機能検査

現在，世界的に使用されている認知症に伴う精神症状を評価する認知検査で日本語版が存在するものとして，情報提供者(介護者)の回答で評価する The Neuropsychiatric Inventory(NPI)[2]，およびその簡易版で 5 分以内に施行可能な The Neuropsychiatric Inventory Questionnaire(NPI-Q)[4]がある．両者は，①妄想，②幻覚，③興奮・攻撃，④憂うつ・不快，⑤不安，⑥意気揚々・多幸，⑦アパシー・無関心，⑧脱抑制，⑨被刺激性・不安定，⑩行為の異常，⑪睡眠，⑫食欲と食行動の異常，の 12 項目について情報提供者にそれぞれの精神症状を尋ねて評価する認知検査である．

最近では，NPI に臨床家が患者面接をして評価する項目を加えた The Neuropsychiatric Inventory Clinician Rating Scale(NPI-C)[3]が作成され，妥当性と信頼性が確認された．NPI-C では情報提供者からの情報に加えて臨床評価が加えられるため，より正確な評価が可能になるというメリットがある一方で，NPI-Q のように簡便に施行できるわけではなく，普及するかどうかは現時点ではわからない．また，患者に関するあらゆる情報および面接から得られた情報などから総合して，各項目の重症度を 0〜3 の 4 段階で主観的に評価するため，訓練されていない臨床家がスコアをつけた場合にはスコアに乖離が生じる可能性がある．

精神症状の評価には熟練した問診の技術がなくてはならないとすると，増え続ける認知症の患者に対応することは困難となってしまう．NPI-Q のように簡便に施行できる認知症に伴う精神症状を評価する認知検査は，今後普及していくと思われる．NPI-Q の日本版である NPI-Q-J を使用ご希望の方は J-ADNI の事務局(center@j-adni.org)にご連絡ください．

3. DSM-Ⅴでの認知症の精神症状の評価

2013 年にアメリカ精神医学会によって DSM-Ⅴが発表される予定であるが，現在のドラフト[1]では，dementia という用語は major neurocognitive disorder に，MCI は minor neurocognitive disorder に置き換えられる予定である．精神症状の評価については，精神病症状，抑うつ，焦燥，攻撃，無関心，徘徊などの有無を 5 桁目にコードする方法や，AD で精神病症状を伴うものと抑うつ症状を伴うものには独立した診断基準を適応する方法などが提唱されている．以下に後者の診断基準を提示する．

① ADで精神病症状を伴うものの診断基準

A．妄想や幻聴や幻視の特徴をもつ

B．精神病症状よりもさきに AD に伴う認知機能障害が生じている

C．持続期間は1カ月を超える．妄想や幻覚は間欠的であってもよく，症状は臨床的に重症であるか機能上の破綻をきたしている

D．せん妄の経過中に現れるものではない

E．物質の直接的な生理学的症状ではなく，統合失調症やほかの精神疾患ではうまく説明されない

② ADで抑うつ症状を伴うものの診断基準

B．大うつ病性障害の10個の症状のうち3個以上の症状が存在する

C．抑うつ症状よりもさきにADに伴う認知機能障害が生じている

D．持続期間は2週間を超え，症状は臨床的に重症である

E．せん妄の経過中に現れるものではない

F．物質の直接的な生理学的症状ではなく，ほかの精神疾患ではうまく説明されない

おわりに

認知症の診断，研究および治験における国際化は著しい．認知症の心理検査も国際化が進んでおり，単に国内で標準化しただけではすまなくなってきている．心理検査の原版と等価な検査を作成し，国際的に通用する診断，分類，重症度の評価を可能にする努力が必要とされているといえよう．

*　　*　　*

文献/URL

1) American Psychiatric Association：DSM-5 Neurocognitive Criteria, Draft 1/7/10, http://www.dsm5.org/Proposed%20Revision%20Attachments/APA%20Neurocognitive%20Disorders%20Proposal%20for%20DSM-5.pdf
2) Cummings, J. L. et al.：The Neuropsychiatric Inventory：comprehensive assessment of psychopathology in dementia. *Neurology*, **44**：2308-2314, 1994.
3) de Medeiros, K. et al.：The Neuropsychiatric Inventory-Clinician Rating Scale (NPI-C). Reliability and validity of a revised assessment of neuropsychiatric symptoms in dementia. *Int. Psychogeriatr.*, **22**：984-994, 2010.
4) Kaufer, D. I. et al.：Validation of the NPI-Q, a brief clinical form of the neuropsychiatric. *J. Neuropsychiatry Clin. Neurosci.*, **12**：233-239, 2000.
5) Kendell, R. E.：Psychiatric diagnosis in Britain and the United States. *Br. J. Hosp. Med.*, **6**：147-155, 1971.
6) Leff, J.：International variation in the diagnosis of psychiatric illness. *Br. J. Psychiatry*, **131**：329-338, 1977.
7) Petersen, R. et al.：Mild cognitive impairment. *Arch. Neurol.*, **66**：1447-1455, 2009.
8) 杉下守弘：認知症テストの現状と展望．*Dementia Japan*, **23**：55-63, 2009.
9) 杉下守弘，朝田　隆：高齢者用うつ尺度—日本版(Geriatric Depression Scale—Short Version-Japanese, GDS-S-J)の作成について．認知神経科学，**11**：87-90, 2009.
10) Weiner, M. F. et al.：Measures of psychiatric symptoms in Alzheimer patients：a review. *Alzheimer Dis. Assoc. Disord.*, **10**：20-30, 1996.

Matsuda et al. BMC Medical Imaging 2010, 10:17
http://www.biomedcentral.com/1471-2342/10/17

BMC Medical Imaging

RESEARCH ARTICLE Open Access

Evaluation of both perfusion and atrophy in multiple system atrophy of the cerebellar type using brain SPECT alone

Hiroshi Matsuda[1*†], Etsuko Imabayashi[1†], Ichiei Kuji[1†], Akira Seto[2], Kimiteru Ito[1], Daisuke Kikuta[1], Minoru Yamada[1], Yasumasa Shimano[1], Noriko Sato[3]

Abstract

Background: Partial volume effects in atrophied areas should be taken into account when interpreting brain perfusion single photon emission computed tomography (SPECT) images of neurodegenerative diseases. To evaluate both perfusion and atrophy using brain SPECT alone, we developed a new technique applying tensor-based morphometry (TBM) to SPECT.

Methods: After linear spatial normalization of brain perfusion SPECT using ^{99m}Tc-ethyl cysteinate dimer (^{99m}Tc-ECD) to a Talairach space, high-dimension-warping was done using an original ^{99m}Tc-ECD template. Contraction map images calculated from Jacobian determinants and spatially normalized SPECT images using this high-dimension-warping were compared using statistical parametric mapping (SPM2) between two groups of 16 multiple system atrophy of the cerebellar type (MSA-C) patients and 73 age-matched normal controls. This comparison was also performed in conventionally warped SPECT images.

Results: SPM2 demonstrated statistically significant contraction indicating local atrophy and decreased perfusion in the whole cerebellum and pons of MSA-C patients as compared to normal controls. Higher significance for decreased perfusion in these areas was obtained in high-dimension-warping than in conventional warping, possibly due to sufficient spatial normalization to a ^{99m}Tc-ECD template in high-dimensional warping of severely atrophied cerebellum and pons. In the present high-dimension-warping, modification of tracer activity remained within 3% of the original tracer distribution.

Conclusions: The present new technique applying TBM to brain SPECT provides information on both perfusion and atrophy at the same time thereby enhancing the role of brain perfusion SPECT

Background

Brain perfusion single photon emission computed tomography (SPECT) has been applied to various neurodegenerative diseases such as Alzheimer's disease. Particular attention must be paid to local atrophy when interpreting brain SPECT images in neurodegenerative diseases, since tracer activity determined by SPECT with limited spatial resolution is greatly influenced by partial volume effects. Local atrophy causes underestimation of tracer activity due to these effects. To precisely evaluate this local atrophy of the brain, magnetic resonance imaging (MRI) has been commonly used. If SPECT could evaluate local atrophy as well as brain perfusion, the role of SPECT would be enhanced in clinical use. In the present study, we developed a new technique to evaluate both perfusion and atrophic changes at the same time using brain SPECT alone, and applied this technique to patients with multiple system atrophy of the cerebellar type (MSA-C) for clinical validation.

Methods

We retrospectively chose 16 patients (9 men and 7 women age 43-75 years, mean ± SD 58.6 ± 8.8) with a clinical diagnosis of probable MSA-C according to the

* Correspondence: matsudah@saitama-med.ac.jp
† Contributed equally
[1]Department of Nuclear Medicine, Saitama Medical University International Medical Center, 1397-1, Yamane, Hidaka, Saitama, 350-1298, Japan
Full list of author information is available at the end of the article

consensus criteria [1]: cerebellar ataxia with additional severe autonomic failure and/or a levodopa-unresponsive or a poorly responsive parkinsonian syndrome. All patients showed characteristic brain MRI findings of cerebellar and pontine atrophy and signal changes in the pons [1,2]. Seventy-three age-matched control subjects (35 men and 38 women; age 43-75 years, mean ± SD 59.6 ± 7.8 years) with no memory impairment or cognitive disorders were recruited as healthy volunteers. The Ethics Committee of the National Center of Neurology and Psychiatry approved this study, and all patients and control subjects gave their informed consent to take part in this study and for their images to be used in a scientific publication. All of the control subjects were right handed and screened by questionnaire and medical history to exclude any with medical conditions potentially affecting the central nervous system. In addition, none of them had asymptomatic cerebral infarction detected by T2-weighted MRI.

All of the subjects underwent brain perfusion SPECT. Before SPECT was performed, an intravenous line was established. Each received a 600 MBq intravenous injection of ^{99m}Tc-ethyl cysteinate dimer (^{99m}Tc-ECD) while lying in the supine position with the eyes closed in a dimly lit, quiet room. Ten minutes after the injection of ^{99m}Tc-ECD, brain SPECT was performed using cameras equipped with high-resolution fanbeam collimators (Multispect3; Siemens Medical Systems, Hoffman Estates, IL). A Shepp and Logan Hanning filter was used as a filtered back-projection method for SPECT image reconstruction at 0.7 cycles/cm. Attenuation correction was performed using Chang's method with an optimized effective attenuation coefficient of 0.09 cm^{-1}.

The present study applied tensor-based morphometry (TBM) to SPECT for the assessment of local atrophy according to the procedure shown in Fig. 1. The basic principle of TBM is to analyze the local deformations of an image and to infer local differences in brain structure [3]. First, a linear spatial normalization algorithm in statistical parametric mapping (SPM2) resized all SPECT images of individual subjects to a voxel size of 2.0 mm and adjusted for orientation, and overall width, length and height. This step transformed brains to the anatomical space of a template brain based on Talairach space. Subsequent non-linear spatial normalization introduced local deformations to each brain to match it to an original template brain for ^{99m}Tc-ECD [4]. This non-linear spatial normalization was done using the high-dimension-warping algorithm [5]. We obtained high-dimensionally warped SPECT images and three-dimensional (3D) deformation fields for every brain using a univariate Jacobian approach. Each of these 3 D deformation fields consists of displacement vectors for every voxel, which describes the 3 D displacement

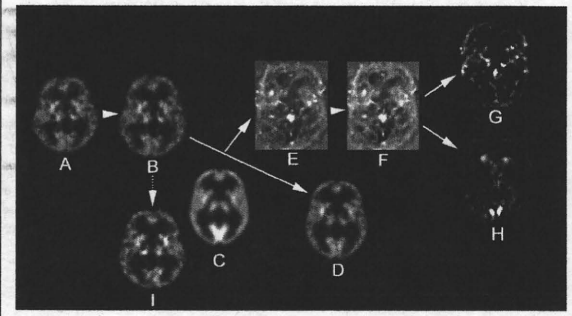

Figure 1 Procedure of tensor-based morphometry using brain SPECT. First, an original SPECT image (A) is linearly transformed to the Talairach space. Subsequent non-linear spatial normalization using the high-dimension-warping algorithm deforms a linearly standardized brain (B) to match it to a ^{99m}Tc-ECD template (C). This step generates a high-dimensionally warped SPECT image (D) and a parametric image of Jacobian determinants (E) indicating a local volume change relative to the template brain. Then the natural logarithm of this parametric image (F) is separated into negative log J (G) and positive log J maps (H) representing contraction and expansion respectively. A conventionally warped SPECT image is also shown (I).

needed to locally deform the brain to match it to the template. We calculated the Jacobian determinants to obtain voxel by voxel parametric maps of local volume change relative to the template brain. The local Jacobian determinant is a parameter commonly used in continuum mechanics, which characterizes volume changes, such as local expansion (Jacobian > 1) or contraction (Jacobian < 1) caused by warping. For more fair comparison of regions showing expansion or contraction, we took the natural logarithm of the Jacobian determinant values (denoted as log J) as reported by Leow et al [6]. Then, parametric maps were separated into negative log J and positive log J maps representing contraction and expansion respectively. Absolute values of negative log J were calculated for further analysis of the contraction maps. A greater absolute value of negative log J indicates severer local atrophy. We also spatially normalized all of the perfusion SPECT images to an original ^{99m}Tc-ECD template brain using a conventional non-linear warping method with 16 iterations of SPM2.

Contraction map images showing the negative J maps with displacement vectors in each voxel, and high-dimensionally and conventionally warped SPECT images were finally smoothed with a Gaussian kernel with FWHM of 10 mm. For statistical inference, these images were analyzed with a general linear model using SPM2. A design matrix was constructed for two-sample t-test between groups of MSA-C patients and normal controls. Inferences were obtained on t-contrasts. P-values used were corrected with familywise error (threshold at $p < 0.05$) depending on the contrast.

Results

A contraction map and high-dimensionally and conventionally warped SPECT images in a representative MSA-C patient are shown with the MRI findings in Fig. 2. Averaged images of the contraction maps and high-dimensionally and conventionally warped SPECT images in the groups of MSA-C patients and normal controls are shown in Fig. 3 and Fig. 4. In the group of MSA-C patients the contraction map images showed greater absolute values of negative log J in the whole cerebellum and pons than in other areas (Fig. 3). Both high-dimensionally and conventionally warped SPECT images showed decreased perfusion in these areas in the group of MSA-C patients as compared to the normal controls (Fig. 4). Functional volume of cerebellum and pons in the averaged images was compared between high-dimensional and conventional warping using a region of interest template of WFU_PickAtlas http://www.nitrc.org/projects/wfu_pickatlas/. In the group of MSA-C patients conventional warping generated 16% and 24% smaller volume of cerebellum and pons respectively than high-dimension-warping. Maximal perfusion ratios of the whole cerebellum and pons to the whole cerebrum were calculated in averaged images also using a region of in-terest template of WFU_PickAtlas. Conventionally warped and high-dimensionally warped SPECT images in the group of MSA-C patients showed maximal perfusion ratios of 0.81 and 0.83 in the whole cerebellum and of 0.55 and 0.58 in the pons on the average respectively. Conventionally warped and high-dimensionally warped SPECT images in the group of normal controls showed maximal perfusion ratios of

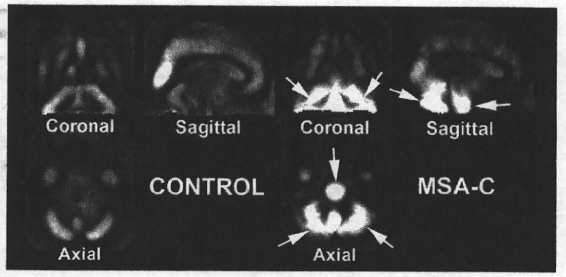

Figure 3 Averaged images of contraction maps calculated from high-dimension-warping in the groups of normal controls and MSA-C patients. In the group of MSA-C patients contraction images showed greater absolute values of negative log J indicating severer atrophy in the whole cerebellum and pons than in other areas (arrows). Normal controls did not show severer atrophy in the cerebellum and pons than in other areas.

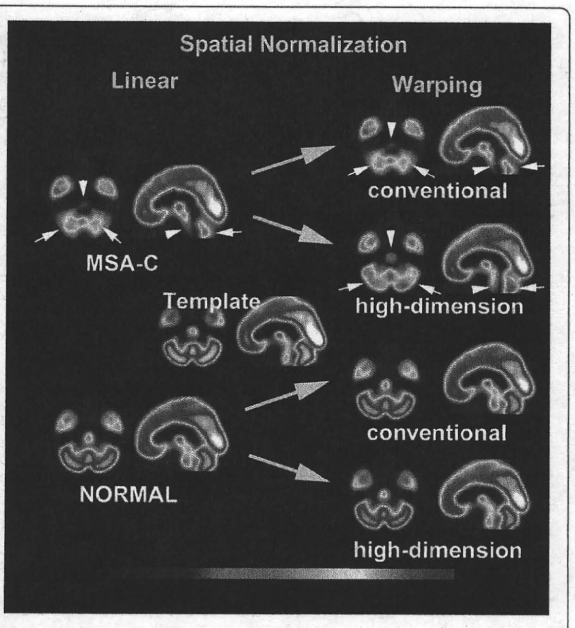

Figure 4 Averaged images of spatially normalized with linear transformation and subsequent conventionally and high-dimensionally warped SPECT images in groups of MSA-C patients and normal controls. Linear spatial normalization showed insufficient transformation to a template in cerebellum (white arrows) and pons (white arrowheads) in MSA-C patients. Subsequent conventional warping could not perform a further transformation in these areas in this group. In contrast, high-dimension-warping could fully transform the cerebellum and pons to a template in MSA-C patients. Both conventionally and high-dimensionally warped SPECT images demonstrated decreased perfusion in the cerebellum and pons in MSA-C patients as compared to normal controls.

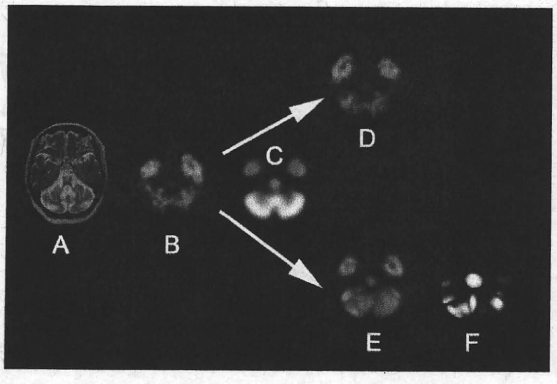

Figure 2 Conventional warping and high-dimension-warping of a SPECT image in an MSA-C patient. T2-weighted MRI (A) showed severe atrophy in cerebellum and pons in a 56-year-old woman with MSA-C. A SPECT image at the level of the pons (B) demonstrated perfusion decrease in the cerebellum and pons. In contrast to conventional warping (D), high-dimension-warping (E) achieved sufficient spatial normalization to a template (C) using a contraction map (F).

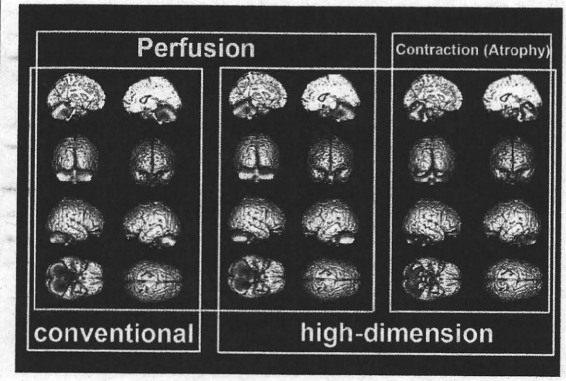

Figure 5 Group comparison of warped SPECT and contraction images between MSA-C patients and normal controls. High-dimension-warping demonstrates significantly decreased perfusion and significant contraction indicating local atrophy as a colored map in the whole cerebellum and pons of MSA-C patients as compared to normal controls. Conventional warping also demonstrated significantly decreased perfusion in the same area as in the high-dimension warping.

0.90 and 0.88 in the whole cerebellum and of 0.68 and 0.65 in the pons on average, respectively.

Group comparisons of these images demonstrated significant contraction indicating local atrophy and decreased perfusion in the whole cerebellum and pons in MSA-C patients as compared to normal controls (Fig. 5 and Table 1). Higher t-values and wider cluster size were obtained with high-dimension-warping as compared to conventional warping.

Table 1 Location of significant perfusion decrease and contraction indicating atrophy in MSA-C patients as compared with normal controls

conventional warping (perfusion)

		Talairach coordinate			
Cluster size	t value	x	y	z	Region
22172	19.9	45	-67	-29	Right Cerebellum, Posterior Lobe
	19.9	-37	-75	-33	Left Cerebellum, Posterior Lobe
	16.9	3	-28	-27	Pons
	14.6	-27	-53	-18	Left Cerebellum, Anterior Lobe
	11.2	30	-43	-30	Right Cerebellum, Anterior Lobe

high-dimension-warping (perfusion)

		Talairach coordinate			
Cluster size	t value	x	y	z	Region
25688	23.2	-49	-58	-34	Left Cerebellum, Posterior Lobe
	22.6	-2	-45	-5	Left Cerebellum, Anterior Lobe
	21.3	34	-75	-33	Right Cerebellum, Posterior Lobe
	21.2	6	-43	-8	Right Cerebellum, Anterior Lobe
	18.8	-2	-21	-24	Pons

high-dimension-warping (atrophy)

		Talairach coordinate			
Cluster size	t value	x	y	z	Region
12947	16.1	-18	-49	-14	left cerebellum, Anterior lobe
	14.2	-4	-73	-27	left cerebellum, Posterior lobe
	12.1	22	-54	-21	Right cerebellum, Anterior lobe
	9.6	46	-72	-22	Right Cerebellum, Posterior Lobe
1416	14.2	-2	-20	-26	Pons

Discussion

The present results of significant perfusion decreases in the cerebellum and pons of the MSA-C patients are the same as those noted in a previous report using SPM analysis of SPECT data with conventional warping [7]. In addition to perfusion data, high-dimension-warping of brain SPECT presented morphological data using a TBM technique. This high-dimension-warping achieves sufficient spatial normalization of locally atrophied areas to a template of Talairach space [5]. This sufficiency was confirmed in severely atrophied cerebellum and pons in the MSA-C patients. Insufficient spatial normalization by conventional warping resulted in a smaller cerebellum and pons than those seen with high-dimension-warping. This better anatomical precision obtained with high-dimension-warping than with conventional warping led to higher significance of the perfusion decrease in the whole cerebellum and pons of the MSA-C patients. A disadvantage of this high-dimension-warping is slight modification of the tracer activity in the original SPECT images in contrast to its preservation in conventional warping. However this modification of tracer activity remained within 3% on the average of the original tracer distribution in the present study.

A TBM technique utilizes information from high resolution deformation tensor fields obtained from the non-linear transformations of individual MRI to the template [8]. This TBM technique was originally used for investigation of longitudinal morphological changes in the same individuals using 3 D volume data of MRI [3,6]. This technique has been recently extended to cross-sectional studies for characterization of morphological changes in specific diseases [9,10]. Prior to high-dimension-warping, there is a need for skull stripping to extract only brain tissue from brain MRI [6]. Incomplete skull stripping substantially deteriorates the precision of high-dimension-warping. This deterioration gives rise to errors in Jacobian determinant values. Unlike MRI data, skull activity is almost negligible in SPECT images. This neglect of skull activity is advantageous to SPECT imaging when applying high-dimension-warping. To the best of our knowledge, this is the first report on application of TBM to brain

perfusion SPECT. This technique succeeded in extracting information on inherent local atrophy from SPECT. Clinical validation could be obtained in the MSA-C patients in the present study because MSA-C manifests a characteristic pattern of atrophy in the whole cerebellum and pons on MRI [2,11]. This characteristic pattern of atrophy was clearly demonstrated by TBM of SPECT.

We must also make note of several study limitations. First, we investigated the applicability of TBM to brain perfusion SPECT in MSA-C patients with severely localized cerebellar and pontine atrophy in the present study. Further investigation on the relationship between atrophy or perfusion changes measured by the present technique and disease severity may be necessary in a larger number of patients. Moreover we have to investigate this applicability in other neurodegenerative diseases with mild atrophy. Second, comparative studies between MRI and SPECT for the evaluation of local atrophy may be necessary for additional validation of this technique. How fine the local atrophy is evaluated may depend on the anatomical precision of a SPECT template. Third, this technique cannot perform partial volume correction in brain perfusion SPECT. However additional information on local atrophy is of great aid in the interpretation of brain perfusion SPECT.

Conclusions

The present technique of application of TBM to brain perfusion SPECT provides information on both local perfusion and atrophy using SPECT alone. The utility of this technique was clinically validated in MSA-C patients as compared to normal controls. Further study is expected on the SPECT data of individual subjects as compared to a normal database of perfusion and atrophy images for routine clinical studies.

Acknowledgements

This work was supported by a Grant-in-Aid for Scientific Research (C) 21591578. from the Ministry of Education, Culture, Sports, Science and Technology of Japan. The authors thank Prof. John Gelblum for English editing of this manuscript.

Author details

[1]Department of Nuclear Medicine, Saitama Medical University International Medical Center, 1397-1, Yamane, Hidaka, Saitama, 350-1298, Japan. [2]Department of Nuclear Medicine, Saitama Medical University Hospital, 38, Morohongo, Moroyama-machi, Iruma-gun, Saitama,350-0495, Japan. [3]Department of Radiology, National Center Hospital of Neurology and Psychiatry, 4-1-1, Ogawahigashi, Kodaira, Tokyo, 187-8551, Japan.

Authors' contributions

HM designed the procedure and the validation protocol of this analysis and drafted the manuscript. EI and IK co-designed the validation protocol and co-drafted the manuscript. AS, KI, YS, and NS performed data analysis in this paper. DK and MY developed a software program for the present analysis. All authors read and approved the final manuscript.

Competing interests

The authors declare that they have no competing interests.

Received: 8 December 2009 Accepted: 11 August 2010
Published: 11 August 2010

References

1. Gilman S, Low PA, Quinn N, Albanese A, Ben-Shlomo Y, Fowler CJ, Kaufmann H, Klockgether T, Lang AE, Lantos PL, Litvan I, Mathias CJ, Oliver E, Robertson D, Schatz I, Wenning GK: **Consensus statement on the diagnosis of multiple system atrophy.** *J Neurol Sci* 1999, **163**:4-5.
2. Watanabe H, Saito Y, Terao S, Ando T, Kachi T, Mukai E, Aiba I, Abe Y, Tamakoshi A, Doyu M, Hirayama M, Sobue G: **Progression and prognosis in multiple system atrophy: an analysis of 230 Japanese patients.** *Brain* 2002, **125**:1070-1083.
3. Gaser C, Nenadic I, Buchsbaum BR, Hazlett EA, Buchsbaum MS: **Deformation-based morphometry and its relation to conventional volumetry of brain lateral ventricles in MRI.** *Neuroimage* 2001, **13**:1140-1145.
4. Ohnishi T, Matsuda H, Hashimoto T, Kunihiro T, Nishikawa M, Uema T, Sasaki M: **Abnormal regional cerebral blood flow in childhood autism.** *Brain* 2000, **123**:1838-1844.
5. Ashburner J, Friston KJ: **High-dimensional image warping.** *Human brain function* San Diego: Elsevier Academic PressFrackowiak RSJ, Friston KJ, Frith CD, Dolan RJ, Price CJ, Zeki S, Ashburner J, Penny W , 2 2004, 673-694.
6. Leow AD, Klunder AD, Jack CR Jr, Toga AW, Dale AM, Bernstein MA, Britson PJ, Gunter JL, Ward CP, Whitwell JL, Borowski BJ, Fleisher AS, Fox NC, Harvey D, Kornak J, Schuff N, Studholme C, Alexander GE, Weiner MW, Thompson PM, ADNI Preparatory Phase Study: **Longitudinal stability of MRI for mapping brain change using tensor-based morphometry.** *Neuroimage* 2006, **31**:627-640.
7. Kawai Y, Suenaga M, Takeda A, Ito M, Watanabe H, Tanaka F, Kato K, Fukatsu H, Naganawa S, Kato T, Ito K, Sobue G: **Cognitive impairments in multiple system atrophy: MSA-C vs MSA-P.** *Neurology* 2008, **70**:1390-1396.
8. Kim J, Avants B, Patel S, Whyte J, Coslett BH, Pluta J, Detre JA, Gee JC: **Structural consequences of diffuse traumatic brain injury: a large deformation tensor-based morphometry study.** *Neuroimage* 2008, **39**:1014-1026.
9. Ohnishi T, Hashimoto R, Mori T, Nemoto K, Moriguchi Y, Iida H, Noguchi H, Nakabayashi T, Hori H, Ohmori M, Tsukue R, Anami K, Hirabayashi N, Harada S, Arima K, Saitoh O, Kunugi H: **The association between the Val158Met polymorphism of the catechol-O-methyl transferase gene and morphological abnormalities of the brain in chronic schizophrenia.** *Brain* 2006, **129**:399-410.
10. Hua X, Leow AD, Parikshak N, Lee S, Chiang MC, Toga AW, Jack CR Jr, Weiner MW, Thompson PM, Alzheimer's Disease Neuroimaging Initiative: **Tensor-based morphometry as a neuroimaging biomarker for Alzheimer's disease: an MRI study of 676 AD, MCI, and normal subjects.** *Neuroimage* 2008, **43**:458-469.
11. Specht K, Minnerop M, Abele M, Reul J, Wüllner U, Klockgether T: **In vivo voxel-based morphometry in multiple system atrophy of the cerebellar type.** *Arch Neurol* 2003, **60**:1431-1435.

Pre-publication history

The pre-publication history for this paper can be accessed here:
http://www.biomedcentral.com/1471-2342/10/17/prepub

doi:10.1186/1471-2342-10-17
Cite this article as: Matsuda *et al.*: **Evaluation of both perfusion and atrophy in multiple system atrophy of the cerebellar type using brain SPECT alone.** *BMC Medical Imaging* 2010 **10**:17.

Original Research Article

Dementia
and Geriatric
Cognitive Disorders

Dement Geriatr Cogn Disord 2010;30:101–111
DOI: 10.1159/000318754

Accepted: June 15, 2010
Published online: August 21, 2010

Voxel-Based Analysis of Amyloid Positron Emission Tomography Probe [^{11}C]BF-227 Uptake in Mild Cognitive Impairment and Alzheimer's Disease

He Shao[a] Nobuyuki Okamura[a] Kentaro Sugi[a] Shozo Furumoto[a, b] Katsutoshi Furukawa[d] Manabu Tashiro[c] Ren Iwata[b] Hiroshi Matsuda[g] Yukitsuka Kudo[f] Hiroyuki Arai[d] Hiroshi Fukuda[e] Kazuhiko Yanai[a]

[a]Department of Pharmacology, Tohoku University Graduate School of Medicine, and Divisions of [b]Radiopharmaceutical Chemistry and [c]Cyclotron Nuclear Medicine, Cyclotron and Radioisotope Center, Tohoku University, and Departments of [d]Geriatrics and Gerontology, Division of Brain Sciences, and [e]Nuclear Medicine and Radiology, Institute of Development, Ageing and Cancer, Tohoku University, and [f]Innovation of New Biomedical Engineering Center, Tohoku University, Sendai, and [g]Department of Nuclear Medicine, Saitama Medical University, International Medical Center, Saitama, Japan

Key Words
Alzheimer's disease · Mild cognitive impairment · Positron emission tomography · Amyloid

Abstract
Aim: To determine early brain changes in the distribution of an amyloid positron emission tomography (PET) probe, ^{11}C-labeled BF-227 or [^{11}C]BF-227, in order to accurately predict the progression of mild cognitive impairment (MCI) to Alzheimer's disease (AD). ***Patients and Methods:*** Amyloid plaque burden was evaluated using [^{11}C]BF-227 PET in AD, MCI and aged normal controls. A voxel-based analysis of [^{11}C] BF-227 PET images was performed to characterize the culprit brain lesion in patients with MCI who were destined to progress to AD, referred to as MCI converters (MCI-C). In addition, binding characteristics of BF-227 to amyloid deposits were examined using postmortem AD brain samples. ***Results:*** Voxel-based statistical analyses of the BF-227 PET images clearly demonstrated an abnormal distribution of BF-227 mainly in the posterior association area in MCI-C and patients with AD. BF-227 uptake in the lateral temporal cortex was consistently observed in almost all MCI-C and patients with AD, and it distinguished MCI-C from MCI nonconverters. BF-227 binding strongly correlated with dense amyloid-β protein plaque density, but not with diffuse plaque density in the frontal cortex. ***Conclusion:*** BF-227 uptake in the lateral temporal cortex is a reliable indicator that can be used for predicting prognosis in patients with MCI.

Introduction

Alzheimer's disease (AD) is considered as the most common cause of dementia in the elderly. Since the extensive deposition of extracellular senile plaques is one of the pathological hallmarks of AD, many researchers have examined these lesions to try and understand the pathogenesis of AD. In 1984, amyloid-β protein (Aβ) was iso-

KARGER

Fax +41 61 306 12 34
E-Mail karger@karger.ch
www.karger.com

1420–8008/10/0302–0101$26.00/0

Accessible online at:
www.karger.com/dem

Nobuyuki Okamura, MD, PhD
Department of Pharmacology, Tohoku University School of Medicine
2-1 Seiryo-machi, Aoba-ku
Sendai 980-8575 (Japan)
Tel. +81 22 717 8058, Fax +81 22 717 8060, E-Mail oka@mail.tains.tohoku.ac.jp

lated from cerebrovascular amyloidosis [1], and in the following year, it was isolated from amyloid plaques and neurofibrillary tangles [2, 3]. Senile plaques, which are mostly composed of Aβ, are believed to accumulate years before the onset of cognitive decline in AD [4]. Ten years ago, the concept of amnestic mild cognitive impairment (MCI) was introduced by the Mayo Clinic group. Amnestic MCI is now considered to be an intermediate predementia stage in patients with AD. Approximately 10–15% of patients with MCI develop AD [5, 6].

Positron emission tomography (PET) imaging using an amyloid-binding agent is a valid method for in vivo evaluation of Aβ plaque burden [7]. Several small molecular amyloid-binding agents have been designed for monitoring amyloid deposits in patients with MCI and AD and for evaluating the efficacy of antiamyloid therapy [8–12]. Furthermore, we have developed several benzoxazole derivatives as potential candidates for amyloid PET probes [13, 14]. A PET study using ^{11}C-labeled BF-227, or [^{11}C]BF-227, successfully detected amyloid plaques in living patients with AD [10]. Recent clinical studies have demonstrated neocortical [^{11}C]BF-227 uptake in patients with MCI [11, 15]. This finding suggests that neocortical [^{11}C]BF-227 uptake could be a potential biomarker for predicting progression from MCI to AD. In previous studies, analysis of PET images was mainly based on analysis of regions of interest (ROI). To eliminate any prior hypothesis about ROI selection, we performed voxel-based analyses of whole brain regions and made comparisons between MCI, AD and aged normal control groups. After [^{11}C]BF-227 PET scanning, we prospectively followed patients with MCI and investigated the relationship between initial BF-227 uptake and prognosis from MCI. The purpose of this study was to explore early changes in the process of amyloid plaque deposition in AD and understand the pattern of neocortical BF-227 distribution for accurate prediction of prognosis in the MCI stage.

Patients and Methods

Subjects and Patients

[^{11}C]BF-227 PET scans were performed on 12 aged normal controls, 19 probable patients with AD and 14 patients with MCI. The patients with AD were recruited via the Tohoku University Hospital Dementia Patients Registry, and the diagnosis was made according to the National Institute of Neurological and Communicative Diseases and Stroke/Alzheimer's Disease and Related Disorders Association criteria [16]. The patients with AD were divided into 2 groups according to their clinical severity: AD1 (Mini-Mental State Examination, MMSE, score ≥20) and AD2 (MMSE score<20). The diagnosis of amnestic MCI was made according to previously published criteria [5], which are as follows: (1) memory complaint, (2) normal activities of daily living, (3) normal general cognitive function, (4) abnormal memory for age, and (5) no sign of dementia. All patients with MCI underwent medical and neuropsychological reevaluation at approximately 3-month intervals and were divided into 2 groups: MCI converters (MCI-C; n = 7) and MCI nonconverters (MCI-NC; n = 7). MCI-C were defined as patients who eventually developed AD within a mean follow-up of 40.0 ± 6.9 months (range: 28–49 months), and MCI-NC were defined as patients having a transient memory loss or remaining cognitively stable for at least 3 years of follow-up (42.4 ± 2.2 months; range: 40–45 months). Aged volunteers who were taking no centrally active medication and who had no cognitive impairment or cerebrovascular lesion on MRI images were recruited as aged normal controls. All aged normal controls were screened via their medical history and responses to the MMSE. Subjects with medical conditions such as multiple cerebral infarctions, normal-pressure hydrocephalus, subdural hematoma, brain tumor, epilepsy, major depression, Parkinson's disease and other neurodegenerative diseases were excluded. In addition, asymptomatic cerebral infarction was not detected on T_2-weighted MRI images in the aged normal controls. The demographic data for all patients and aged normal controls are shown in table 1. The protocol of this study was approved by the Committee on Clinical Investigation at the Tohoku University School of Medicine, and by the Advisory Committee on Radioactive Substances at Tohoku University. Written informed consent was obtained from all patients and controls after complete description of the study. The clinical study was performed in accordance with the Declaration of Helsinki.

Radiosynthesis

BF-227 and its N-desmethylated derivative, a precursor to [^{11}C]BF-227, were synthesized by Tanabe R&D Service Co. (Osaka, Japan). [^{11}C]BF-227 was synthesized from the precursor by N-methylation in dimethyl sulfoxide, using [^{11}C]methyl triflate [10]. After quenching the reaction with 5% acetic acid in ethanol, [^{11}C]BF-227 was separated from the crude mixture by semipreparative, reversed-phase high-performance liquid chromatography and isolated from the collected fraction by solid-phase extraction. Purified [^{11}C]BF-227 was solubilized in isotonic saline containing 1% polysorbate 80 and 5% ascorbic acid. The saline solution was filter sterilized with a 0.22-μm Millipore filter (Millipore Co., Bedford, Mass., USA) for clinical use. At the end of synthesis, the radiochemical yields were greater than 50%, based on [^{11}C]methyl triflate, and the specific radioactivity ranged from 119 to 138 GBq/μmol. Radiochemical purities were greater than 95%.

Scanning Protocol

The [^{11}C]BF-227 PET study was performed using a SET-2400W PET scanner (Shimadzu, Kyoto, Japan). After intravenous injections of 211–366 MBq [^{11}C]BF-227, dynamic PET images were obtained for 60 min (23 sequential scans; 5 scans × 30 s, 5 scans × 60 s, 5 scans × 150 s, and 8 scans × 300 s) with closed eyes. All aged normal controls and patients underwent MRI using a 1.5-tesla MRI scanner (GE Signa Hispeed; GE Healthcare, Milwaukee, Wisc., USA). A 3-D volumetric acquisition of a T_1-weighted gradient echo sequence produced a gapless series of thin axial sections, using a vascular time-of-flight spoiled gradient echo sequence

Table 1. Demographic information on all the subjects

	Aged normal	MCI-NC	MCI-C	AD1	AD2	All AD
Number	12	7	7	10	9	19
Age, years	67.3 ± 2.7 (64–71)	77.6 ± 3.1* (74–82)	79.4 ± 4.2* (75–85)	72.9 ± 5.4 (65–85)	72.6 ± 7.3 (61–82)	72.7 ± 6.2 (61–85)
Gender (F/M), n	6/6	5/2	3/4	2/8	4/5	6/13
MMSE score	29.9 ± 0.3 (29–30)	26.3 ± 1.1 (25–28)	24.6 ± 3.4 (23–29)	22.7 ± 1.4* (21–25)	17.2 ± 2.9*, # (12–20)	20.1 ± 3.6 (12–25)
Years of education	13.2 ± 0.94	12.3 ± 0.48	11.9 ± 0.55	10.9 ± 0.72	10.3 ± 0.65	10.5 ± 0.42
GDS score	4.01 ± 0.44	4.32 ± 0.34	4.79 ± 0.31	4.23 ± 0.35	4.18 ± 0.46	4.20 ± 0.28

Values denote means ± SD with ranges in parentheses unless stated otherwise. Kruskal-Wallis test followed by Dunn's multiple comparison test. GDS = Geriatric Depression Scale. * $p < 0.05$ versus aged normal, # $p < 0.05$ versus MCI-NC.

(echo time/repetition time: 2.4/50 ms; flip angle: 45°; acquisition matrix: 256 × 256; 1 excitation; field of view: 22 cm; slice thickness: 2.0 mm).

Image Analysis

Standardized uptake value (SUV) images of [^{11}C]BF-227 were obtained by normalizing tissue concentration to injected dose and body weight. Average summations of SUV images were created from frames (20–40 min after injection) of dynamic PET images. Individual MR images were anatomically correlated with BF-227 PET images, using a statistical parametric mapping software (SPM5; Wellcome Department of Imaging Neuroscience, London, UK) [17]. ROI in the frontal cortex (Brodmann's areas, BA, 8, 9, 10, 44, 45, 46 and 47), lateral temporal cortex (BA 21, 22, 37 and 38), parietal cortex (BA 39 and 40), occipital cortex (BA 17), posterior cingulate cortex (BA 31) and cerebellar hemisphere were superimposed on MRI images, as described previously [10]. ROI information was then copied onto PET images, and regional SUV values at 20–40 min after injection were sampled using Dr. View/LINUX software (AJS, Tokyo, Japan). The cerebellum was used as the reference region. The regional-to-cerebellum SUV ratio (SUVR) was calculated and used as an index of BF-227 retention because the cerebellum is reported to be a region free of fibrillar amyloid plaques in the AD brain. Voxel-by-voxel comparisons between images from aged normal controls, patients with MCI and patients with AD were performed using SPM5 software. Spatial normalization was performed using an MR T_1 template of SPM5 to transfer PET images onto a standard stereotactic space. The normalized PET images were smoothed, using a 12 × 12 × 12 mm gaussian filter. The voxel count was normalized to the cerebellar ROI value. Images of the MCI-NC, MCI-C and AD groups, including patients with AD1 and AD2, were compared with those of the aged normal controls by means of a between-group analysis ($p < 0.05$ with false discovery rate correction; extent threshold: $k = 750$). For group analysis, a two-sample t test was used to detect differences among the groups.

In addition, a Z-score map of individual PET images was created for comparison between the mean and SD of the PET images of aged normal controls for each voxel. A software program named the Easy Z-Score Imaging System was used for this analysis [18]. Each PET SUV image was compared with the mean and SD of PET images of 15 aged normal controls (age: 58.9 ± 13.5 years; gender M/F: 10/5; MMSE score: 29.9 ± 0.2), using voxel-by-voxel Z-score analysis following voxel normalization to cerebellar ROI values according to the following formula: Z-score = (control mean – individual value)/control SD. Z-score maps were displayed by projection, with an averaged Z-score of 14 mm thickness to the surface rendering the anatomically standardized MRI template.

Neuropathological Staining

Postmortem brain tissue from an autopsy-confirmed AD case (87-year-old male) was obtained from the Tohoku University Hospital. Serial sections (6 μm thick) of paraffin-embedded blocks of temporal and frontal cortices were prepared in xylene and ethanol. Before staining, quenching of autofluorescence was performed by blanched sections in 0.25% potassium permanganate solution for 30 min. The sections were then treated with 0.1% potassium metabisulfite and 0.1% oxalic acid, followed by dipping briefly in water. The quenched tissue sections were immersed in 100 μmol/l of compound solution for 10 min and examined using a BX-51 fluorescence microscope (Olympus, Tokyo, Japan) equipped with a violet filter set (excitation: 380–420 nm; dichroic mirror: 430 nm; long-pass filter: 450 nm). Immunostaining was performed using monoclonal antibodies against Aβ (6F/3D; Dako, Glostrup, Denmark) at a dilution of 1:50. After pretreatment with formic acid for 5 min, the sections were placed in blocking solution for 30 min. After incubation with primary antibodies at 37°C for 60 min, the sections were processed by the avidin-biotin method using the Pathostain ABC-POD(M) kit (Wako) and chromogen DAB. The amyloid plaque morphology was classified into 2 types: (1) dense Aβ plaques including cored deposits with or without a ring of neuritic fibers, and (2) diffuse Aβ plaques including amorphous deposits. We randomly selected 20 areas (1.05 mm^2 per area) per section in the gray matter of the frontal and temporal cortices and counted the number of dense and diffuse Aβ plaques in each area. To estimate the capability of the compound to detect each kind of plaque, we examined the relationship between the number per unit area of positive staining using BF-227- and Aβ-specific antibody.

Statistical Analysis

Statistical comparisons of age among the 5 groups were performed using the Kruskal-Wallis test followed by Dunn's multiple comparison test. Statistical comparison of ROI results was performed via an analysis of variance followed by the Bonferroni method for multiple comparisons. Furthermore, effect size coefficients (Cohen's d) were calculated to evaluate group differences in PET measurements. The performance of diagnostic indices to

discriminate among groups was assessed using receiver operating characteristic (ROC) analysis. The area under the ROC curve (AUC) and SE were calculated and compared using GraphPad Prism software (GraphPad, San Diego, Calif., USA). Correlations between stainability of Aβ immunostaining and BF-227 staining were examined using the nonparametric Spearman rank correlation analysis. The paired t test was used to examine the difference in cored plaque density between the frontal and temporal cortices. Statistical significance for each analysis was defined as $p < 0.05$. These analyses were performed using GraphPad Prism software.

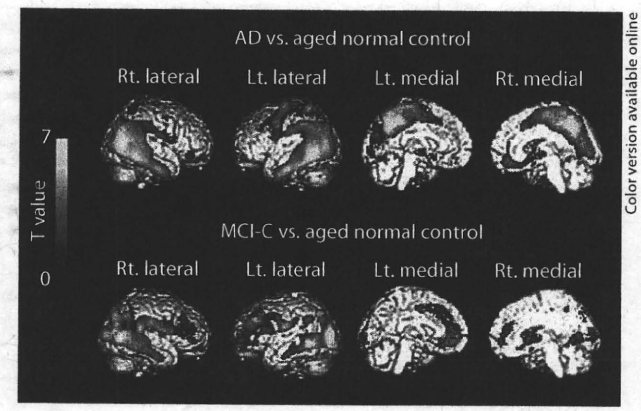

Fig. 1. Brain regions showing significantly higher uptake of [^{11}C] BF-227 in patients with AD (upper images) and MCI-C (lower images) compared with data from aged normal controls ($p < 0.05$, corrected for multiple comparisons). The red-to-yellow scale indicates the level of statistical significance of the differences in [^{11}C]BF-227 uptake (yellow: most significant difference).

Results

A statistically significant difference in age between aged normal controls and patients with MCI ($p < 0.05$) was observed. However, no statistically significant difference in age between MCI-C and MCI-NC as well as between aged normal controls and patients with AD was observed. Patients with AD showed a significantly lower MMSE score than aged normal controls. In addition, the AD2 group showed a significantly lower MMSE score than the MCI-NC group. However, no statistically significant difference in MMSE score was observed among other groups.

Voxel-based analysis of [^{11}C]BF-227 PET images demonstrated that MCI-C and patients with AD had significantly higher [^{11}C]BF-227 uptake in the neocortical region than aged normal controls (fig. 1; tables 2, 3). Bilateral temporoparietal BF-227 uptake was evident in both the AD and MCI-C groups although significant uptake in the posterior cingulate cortex and precuneus was observed only in the AD group. In the AD and MCI-C groups, the difference in the lateral frontal cortex was less evident compared with that in the lateral temporoparietal region. In contrast to the MCI-C group, the MCI-NC group showed no significant elevation of BF-227 uptake compared with the aged normal control group. Z-score maps of PET images were created by comparison with the normal control database (fig. 2). Most patients with AD showed a Z-score greater than 2 in the bilateral temporal and posterior cingulate cortices. In contrast, 10 out of the 12 aged normal controls (83%) showed no remarkable change in neocortical BF-227 uptake, except for 2 subjects (17%) showing modest changes in the lateral temporal and cingulate cortices. MCI-C tended to show higher neocortical Z-scores than MCI-NC (fig. 2b). Among the 7 MCI-C, 4 showed BF-227 uptake in the bilateral temporoparietal and frontal cortices, while the other 2 showed moderate abnormality in the temporal and frontal Z-scores. In MCI-C, changes in BF-227 uptake within the posterior cingulate cortex were relatively moderate compared with those in the lateral temporal cortex. One MCI-C showed limited change in BF-227 uptake within the temporal cortex and precuneus. In contrast to MCI-C, most MCI-NC showed no abnormal BF-227 uptake in the lateral temporal cortex, except for 1 who showed a slightly higher Z-score in the temporal cortex and an extremely high score in the posterior cingulate cortex. Another 3 MCI-NC also showed limited abnormality in the posterior cingulate cortex and precuneus but no abnormal Z-score in the lateral temporal cortex. No significant difference in BF-227 uptake was observed between the MCI-NC and MCI-C groups, MCI-NC and AD groups, and MCI-C and AD groups. Furthermore, no significant region showing reduction in BF-227 uptake in the MCI and AD groups compared with the aged normal controls was observed.

ROI analysis data were roughly consistent with voxel-based analysis data (fig. 3; table 4). The MCI-C group showed higher retention of [^{11}C]BF-227 in the frontal, temporal and parietal cortices than the aged normal control group. The AD1 group showed higher BF-227 retention in the frontal, temporal, parietal and occipital cortices than the aged normal control group. The AD2 group showed higher BF-227 retention in the temporal, parietal, occipital and posterior cingulate cortices than the aged normal control group, with the exception of the frontal cortex. Furthermore, significantly higher BF-227 uptake

Table 2. Talairach coordinates of within-cluster peak areas showing significantly higher BF-227 uptake in AD patients compared with aged normal group ($p < 0.05$, false discovery rate corrected)

k	T value	Talairach coordinates			Region
		x	y	z	
48,058	7.15 (5.38)	54	−46	−12	right inferior temporal gyrus
	6.79 (5.21)	50	−62	14	right middle temporal gyrus
	6.22 (4.92)	−52	−58	−2	left middle temporal gyrus
760	4.81 (4.09)	−24	4	−4	left putamen

Values in parentheses denote Z values.

Table 3. Talairach coordinates of within-cluster peak areas showing significantly higher BF-227 uptake in MCI-C compared with aged normal group ($p < 0.05$, false discovery rate corrected)

k	T value	Talairach coordinates			Region
		x	y	z	
14,893	6.19 (4.42)	46	−64	6	right middle temporal gyrus
	5.84 (4.27)	40	−74	14	right middle temporal gyrus
	5.52 (4.12)	52	−44	−8	right temporal lobe subgyrus
6,768	5.78 (4.24)	−36	32	34	left middle frontal gyrus
	4.78 (3.75)	−58	−16	24	left parietal lobe
	4.70 (3.71)	−24	50	0	left superior frontal gyrus
5,893	5.77 (4.24)	−38	−80	10	left middle occipital gyrus
	5.52 (4.12)	−42	−60	−4	left middle temporal gyrus
	5.27 (4.00)	−22	−92	−4	left cuneus

Values in parentheses denote Z values.

was found in the frontal and temporal cortices of the MCI-C group as well as in the temporal and parietal cortices of the AD group compared with the MCI-NC group. Compared with the AD group, Cohen's d was higher in the temporal (2.93) and parietal (2.25) cortices than in the frontal (1.69) and posterior cingulate (1.51) cortices for the aged normal control group. When comparing the MCI-C and MCI-NC groups, the highest Cohen's d was observed in the temporal (1.70) and parietal (1.76) cortices, followed by the frontal (1.62), posterior cingulate (0.85) and occipital (0.37) cortices, indicating that the difference in SUVR is the largest in the temporoparietal cortex when comparing the MCI-C and MCI-NC groups. Furthermore, ROC analysis demonstrated higher AUC values with the temporal SUVR (AUC = 0.987; SE = 0.016) than with the frontal SUVR (AUC = 0.915; SE = 0.052) for the discrimination between the AD and aged normal control groups as well as between the MCI-C and MCI-NC groups (fig. 4). Using the temporal BF-227 SUVR of 1.10 (1.5 SD above control mean) as the cutoff, a sensitivity of 95% and specificity of 92% in the discrimination between AD and aged normal groups, and a sensitivity of 100% and specificity of 57% in the discrimination between MCI-C and MCI-NC was achieved.

To explain why BF-227 preferentially accumulates in the temporal cortex as opposed to the frontal cortex of the AD brain, we examined the binding characteristics of BF-227 to Aβ deposits, using postmortem AD brain samples. BF-227 showed good stainability for dense-type plaques in the frontal and temporal cortices. Diffuse plaques in the frontal cortex tended to be larger than those in the temporal cortex. However, the stainability for diffuse-type plaques in the frontal cortex was relatively weaker than that in the temporal cortex (fig. 5). The mean number of Aβ plaques positively stained with BF-227 was significantly higher in the temporal cortex than in the fron-

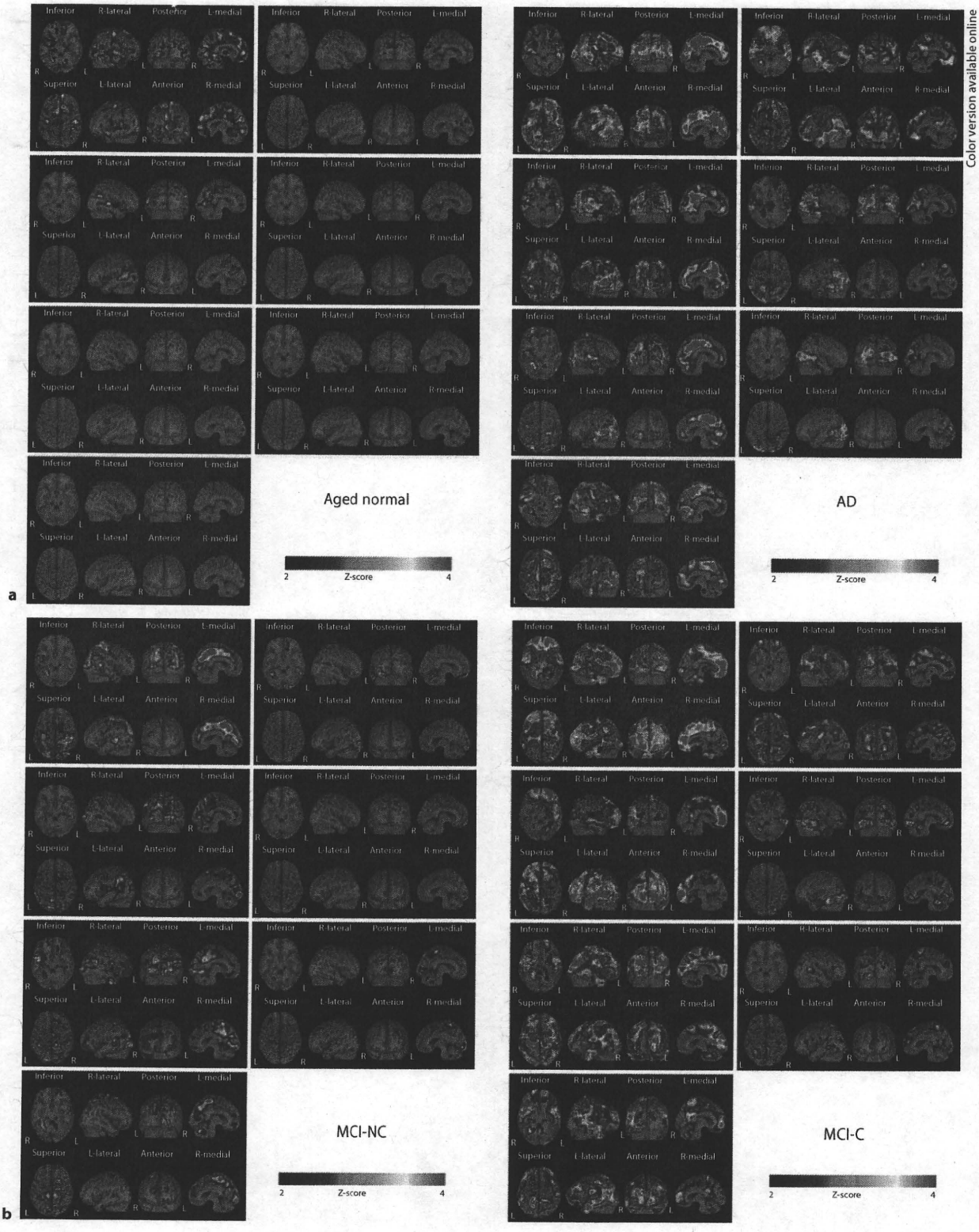
Color version available online
a
Aged normal
AD
2
Z-score
4
b
MCI-NC
MCI-C
2
Z-score
4